

# Stochastic Model-Based Contact Force Estimation for Concentric Tube Robots

Mahdi Pourafzal<sup>a</sup>, Ali Talebi<sup>a,\*</sup> and Kanty Rabenoroso<sup>b</sup>

<sup>a</sup>Department of Electrical Engineering, Amirkabir University of Technology, Tehran 15914, Iran

<sup>b</sup>FEMTO-ST Institute, Univ. Bourgogne Franche-Comté, CNRS, F-25000 Besançon, France

## ARTICLE INFO

### Keywords:

Concentric tube robots, External load, Force estimation, Stochastic kinematics, Piece-wise constant strain kineto-static model.

## ABSTRACT

This work utilizes a Wiener process to describe a fluctuating load on a Concentric tube robot (CTR) or its smooth motion through fixed obstacles leading to a kineto-static piecewise constant strain (KPCS) model. We then propose an observer based on the KPCS model, represented as a stochastic switched system, to estimate the externally applied forces by knowing the position of discrete points on the backbone. We have demonstrated that the observer describes the behavior of CTRs in unknown constraint environments and slow movement. The experiments carried out using electromagnetic sensors on the CTR prototype validate the feasibility of the proposed approach for shape and tip-force estimation. The average time required for force estimation is about 3.8, 6.2, and 20 ms per sample, respectively, when the estimated external forces are applied on a three-tube CTR's tip point and three and fifteen equally spaced points along its length. The implementation results reveal the estimated force reduces the error of the robot tip position by half (about 1.5% of the robot length on average) compared to the known external force.

## 1. Introduction

Concentric tube robots (CTRs) are an emerging robotic surgical platform consisting of multiple, pre-curved, compliant elastic tubes arranged in a telescopic manner. Their small size and flexible design make them ideal for skillful surgical maneuvers, allowing a safer minimally invasive surgery (MIS) inside delicate and confined environments [1, 2, 3]. They can be steered in a Follow-The-Leader manner [4] maintaining their performance despite tool-tissue interaction force. It gives the surgeon the ability to perform many complicated, challenging, and sophisticated surgeries, such as intracardiac procedures [5] and endonasal skull base surgery [6]. To achieve such a target, shape deformations due to unknown loads from collisions with anatomy must be fully modeled.


The deployment of CTRs in medical procedures requires position and force control of the distal tip that interacts with the tissue [7, 8]. Thus the perception of external forces is an essential prerequisite for their practical use. The structural flexibility and compactness of CTRs pose a significant challenge in equipping them with force sensors [9]. Fortunately, continuum robots can provide a promising solution for indirect force-sensing methods through their compliance structure. This feature referred to as intrinsic force-sensing capability, gives us the chance to use the robot itself as a sensor and estimate external loads reasonably by using backbone deflection [10] or joint-level information [11, 12]. Therefore the discrete points along a backbone can be a valuable source detectable by various sensing methods [13]. Electromagnetic (EM) trackers are a standard medical sensing

method [14] adopted for CTRs that directly provide such information. Another popular approach that could efficiently integrate with CTRs is fiber Bragg grating (FBG). The shape reconstruction techniques based on this approach rely on curvature estimation through strain sensing and provide the ability to obtain the position data of any arbitrary point of backbone. [15, 16].

A considerable amount of literature deals with using backbone position information to estimate external forces acting on it. However, the majority of them are devoted to planar continuum robots. The pose measurement of a steerable catheter tip has been used in [17] to estimate the applied external forces when it came into contact with heart tissue in an ablation operation. A series of piecewise circular arcs parameterize the catheter backbone curve and create a low-dimensional model in quasi-static conditions. In [18], the information gained from a catheter curvature gave the loading status and allowed defining an index for determining the range of contact forces. Moreover, in [19], a force estimation method based on planar Cosserat modeling and catheter shape detection has been proposed to reduce the high order PDEs into a set of linear system equations by making several assumptions. A probabilistic approach based on tip pose measurements and actuation torques has been presented in [20] for the force estimation of continuum robots.

Nevertheless, contact force estimation is more challenging for the robots undergoing out-of-plane deformations. A pseudo rigid body approach has been presented in [21] to estimate the reaction forces and predict the deformed shape of a magnetically actuated continuum manipulator in 3D, while stereo-vision techniques sense its position. The 3D shape estimation of CTRs based on fluoroscopic images has been addressed in [22], where an energy minimization approach based on the Markov random field unified the task of 2-D tracking and 3-D shape reconstruction. A model-

\*Corresponding author

 m.pourafzal@aut.ac.ir (M. Pourafzal); alit@aut.ac.ir (A. Talebi); kanty.rabenoroso@femto-st.fr (K. Rabenoroso)

<sup>1</sup>The work of K. Rabenoroso was supported by the EIPHI Graduate School (ANR-17-EURE-0002) and ANR  $\mu$ RoCS (ANR-17-CE19-0005).

based force estimation approach was presented in [23] for a flexible medical instrument. It employed FBG sensors and an extended Kalman filter to realize the real-time shape and force sensing. A recurrent neural network has been used in [24] to provide a real-time tip contact force estimator for a tendon-driven continuum manipulator. In [10], a data-driven approach based on Deep Direct Cascade Learning has been proposed to create a force-from-shape sensor and estimate CTRs' tip contact force in the 3D workspace through backbone deflection. Even though data-based approaches share attractive characteristics like high accuracy and low computation time, they entirely depend on reliable training data and have low interpretability. Therefore, model-based shape and force estimation facilitates the successful control and stability assurance [25, 26, 27] of CTRs under loading conditions.

A model-based force estimation approach demands a suitable model describing the robot's behavior in confined spaces and providing low computational cost and high performance. In recent years, efforts have been made to reduce the kinematic computation time of continuum and soft robots, traditionally coupled to Cosserat models [28, 29]. Some of these attempts are based on piecewise constant strain (PCS) and have led to computationally efficient models for soft manipulators [30, 31]. They discretize the robot length into pieces with constant deformation and, despite decreasing computational burden, allow including shear and torsional strains crucial in dealing with out-of-plane deformations.

This paper enables a model-based estimation of external loads applied to CTRs. To the best of our knowledge, this is the first time the Wiener process has been used to describe the external force on CTR in quasi-static conditions. We use the PCS kinematic model of CTRs presented in [32] and further consider external loads acting on the backbone as a set of point forces described by Wiener processes. A stochastic observer estimates their mean values, while the variances have been considered proportional to the distal torsions. The remainder of the paper is organized as follows. Section 2 presents the basic notations and assumptions. In the third section, we briefly recall the PCS kinematic model presented for CTRs. Section 4, based on stochastic modeling and estimation techniques, offers the kineto-static piecewise constant strain (KPCS) model of CTR and the external force estimation approach. Section 5 shows the results of simulation and experiment to validate the proposed method, and finally, the conclusion appears in section 6.

## 2. Basics and Assumptions

This paper uses the following notation:  $s$  is the arc-length parameter so that  $s > 0$  is related to the exterior part of the CTR, and  $s < 0$  corresponds with its actuation part, as given in Fig. 1.  $[a]_{\times}$  indicates the skew-symmetric matrix of vector  $a$ .  $\Delta x_{(i,j)}$  represents  $x_{(i,j+1)} - x_{(i,j)}$ .  $\bar{\lambda}(\cdot)$  and  $\underline{\lambda}(\cdot)$  denote the maximum and minimum eigenvalues of a symmetric matrix. Moreover, throughout the paper, we make the following assumptions. A1) Tubes are supposed to bend

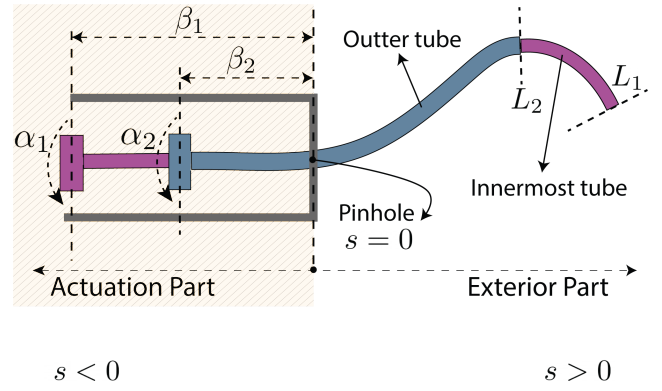


**Figure 1:** Diagram showing actuation and exterior parts of a two-tube CTR, where actuation variables  $\alpha_i$  and  $\beta_i$ , respectively, denote the proximal base rotation and translation of the  $i$ th tube.

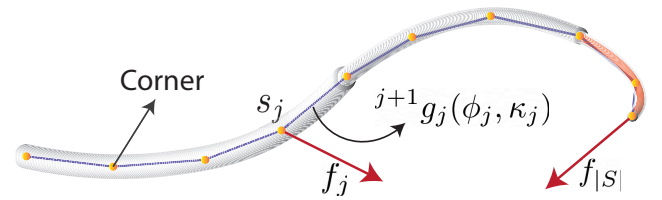


**Figure 2:** Schematic of a CTR described by the PCS model and external forces.

or twist elastically but do not undergo cross-section shear and axial elongation by respecting the Kirchhoff hypothesis. This assumption is generally reasonable for long thin rods like the tubes [33]. A2) The stiffness of tubes in bending and torsion is assumed to be linear elastic. A3) External loading is exclusive to a set of point forces exerted at the backbone, and as a result, external moments and distributed forces are neglected. It also makes sense that friction among the tubes is assumed quite negligible. A4) Tubes are divided into pieces with constant strain over which the curvature and torsion are constant. A5) The position of discrete points on the CTR, where external forces are applied, is known. A6) The external forces are assumed to be quasi-static and modeled by a set of Wiener processes, the means of which are unknown.

## 3. PCS Kinematic Model of CTRs

This section [overviews](#) of the PCS kinematic model [32] of CTRs. Let  $i = 1 \dots n$  denote the number of the not fully overlapped tubes of a CTR numbered from the innermost to the outermost, dividing the robot length into  $n$  sections. [Each section of the CTR's exterior part](#) is divided into  $h_i$  helical pieces. They are arranged in series, indexed from the backbone proximal end to the distal one, and connected at the points of set  $S$  known as corners, the position of which is denoted by  $p_j (j = 1 \dots |S|)$ . The lengths of [tube  \$i\$  and pieces  \$j\$  are given by  \$L\_i\$  and  \$l\_j\$](#) . The external loading is represented as force set  $F = \{f_1 \ f_2 \ \dots \ f_{|S|}\}$ , in which  $f_j$  is the point force acting on corner  $s_j \in S$  (see Fig. 2). The input (actu-

ator) vector is denoted by  $\mathbf{q} = [\alpha_1 \ \beta_1 \ \dots \ \alpha_n \ \beta_n]$ , where  $\alpha_i$  and  $\beta_i$ , as shown in Fig.1, are the rotation and translation angle of tube  $i$  at the base. The internal moments at arc-length  $s_j$  are obtained using

$$\begin{bmatrix} m_x(s_j) \\ m_y(s_j) \end{bmatrix} = R_B^T(s_j) \sum_{k>j} ([\mathbf{p}_k]_{\times} - [\mathbf{p}_j]_{\times}) \mathbf{f}_k \Big|_{x,y} \quad (1)$$

and

$$m_{z_i}(s_j) = \mathbf{e}_3^T R_B^T(s_j) \sum_{j<k<m_1+\dots+m_i} ([\mathbf{p}_k]_{\times} - [\mathbf{p}_j]_{\times}) \mathbf{f}_k \quad (2)$$

in which  $\mathbf{e}_3 = [0 \ 0 \ 1]$ , and  $R_B(s)$  is a rotation matrix from base to body Bishop frames assigned along the CTR. Given assumption A1, the constant strain vector of a torsionless centerline can be specified by

$$\boldsymbol{\zeta}_j = [e_3^T - \kappa_j \sin \phi_j \ \kappa_j \cos \phi_j \ 0]^T \quad (3)$$

in which  $\kappa_j$  and  $\phi_j$  are the curvature and bending angle at  $s_j \in \mathcal{S}$  obtained from

$$\begin{bmatrix} \kappa_{x_j} \\ \kappa_{y_j} \end{bmatrix} = \frac{1}{\sum_{i=1}^{n_j} E_i I_i} \left( \sum_{i=1}^{n_j} E_i I_i \kappa_i^* \begin{bmatrix} \sin \theta_{i,j} \\ \cos \theta_{i,j} \end{bmatrix} + \begin{bmatrix} -m_x(s_j) \\ m_y(s_j) \end{bmatrix} \right) \\ \kappa_j = \sqrt{\kappa_{x_j}^2 + \kappa_{y_j}^2}, \quad \phi_j = \tan^{-1}(\kappa_{x_j}/\kappa_{y_j}) \quad (4)$$

where  $\kappa_i^*$  is pre-curvature,  $E_i$  is Young's modulus,  $I_i$  is the area moment of inertia of the tube cross-section, and  $\theta_{i,j}$  denotes the twist angle of the  $i$ th tube at the  $j$ th corner given as

$$\theta_{i,j} = \theta_{i,j-1} + \tau_{i,j-1} L_{i,j} \quad (5)$$

As it is shown in Appendix A, the elastic energy stored along the tubes is minimized if torsion  $\tau_{i,j}$ , for  $s \geq 0$ , fulfills the following condition

$$\tau_{i,j+1} = \tau_{i,j} - \frac{E_i I_i}{G_i J_i} \kappa_j \kappa_{i,j}^* L_{i,j} \sin(\phi_j - \theta_{i,j}) + \Delta \tau_{e(i,j)}^* \quad (6)$$

where  $\tau_{e(i,j)}^* = m_{z_i}(s_j)/G_i J_i + \tau_{i,j}^*$ , in which  $\tau_{i,j}^*$  is pre-torsion,  $G_i$  is shear modulus, and  $J_i$  denotes the polar moment of inertia of the  $i$ th tube. For  $s < 0$

$$\theta_{i,1} = \alpha_i + \int_{-\beta_i}^0 (\tau_{i,1} + \tau^*(\mu)) d\mu \quad (7)$$

The PCS forward kinematics map at corner  $j$  can be given by the product of exponential formula as

$$\mathbf{g}_j = \begin{cases} \prod_{k=1}^{j-1} e^{\hat{\boldsymbol{\zeta}}_k L_k} & j = 2, \dots, |S| \\ I_4 & j = 1 \end{cases} \quad (8)$$

According to (2), internal moments  $m_{z_i}(s)$  are zero at the tubes' distal points, and the torsions must also be zero there. Drawing the robot's actual shape is only possible by finding the proximal torsion fulfilling the distal torsion constraint.

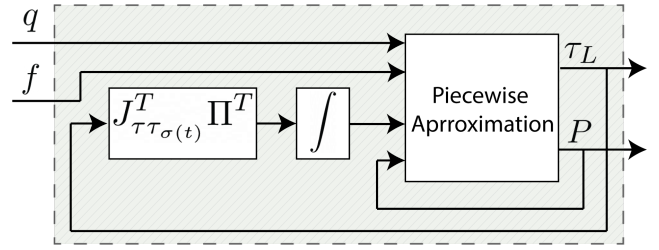


**Figure 3:** Block diagram of the PCS kinematic model for CTRs in which  $\mathbf{F}$ ,  $\mathbf{q}$  are the set of external forces and actuator vector. Output  $\mathbf{P}$  which includes the position of corner points feedbacked into the input.

The PCS approximation explained can be summarized in the following functions

$$\boldsymbol{\tau}_L = \boldsymbol{\chi}(\mathbf{q}, \mathbf{F}, \mathbf{P}, \boldsymbol{\tau}_0), \quad \mathbf{P} = \boldsymbol{\xi}(\mathbf{q}, \mathbf{F}, \mathbf{P}, \boldsymbol{\tau}_0) \quad (9)$$

where  $\mathbf{P} = \{\mathbf{p}_1 \ \mathbf{p}_2 \ \dots \ \mathbf{p}_{|S|}\}$  involves the positions of corners and  $\boldsymbol{\tau}_0 = [\tau_{1,1} \ \tau_{2,1} \ \dots \ \tau_{n,1}]^T$  is the proximal torsion vector. Moreover, output  $\boldsymbol{\tau}_L$  in (9) is a vector containing distal torsions.

$$\boldsymbol{\tau}_L = [\tau_{1,h_1} \ \tau_{2,h_1+h_2} \ \dots \ \tau_{n,|S|}]^T \quad (10)$$

One can interpret the searching for a proximal torsion (input) satisfying the distal torsion (output) condition as internal feedback. In this intention, the corners' position in the output is fed directly back into the input (see Fig. 3), and the torsion feedback is obtained from the following theorem to determine the ultimate shape of the CTR.

**Theorem 1** ([32]). *Let proximal torsion vector  $\boldsymbol{\tau}_0$  is updated by*

$$\dot{\boldsymbol{\tau}}_0 = -\gamma \mathbf{J}_{\tau\tau\sigma(t)}^T \boldsymbol{\Pi}^T \boldsymbol{\tau}_L$$

where  $\mathbf{J}_{\tau\tau\sigma(t)} = \frac{\partial \boldsymbol{\chi}(\cdot)}{\partial \boldsymbol{\tau}_0} + \boldsymbol{\Gamma} \frac{\partial \boldsymbol{\xi}(\cdot)}{\partial \boldsymbol{\tau}_0}$ ,  $\boldsymbol{\Gamma} = \frac{\partial \boldsymbol{\chi}(\cdot)}{\partial \mathbf{P}} (\mathbf{I} - \frac{\partial \boldsymbol{\xi}(\cdot)}{\partial \mathbf{P}})^{-1}$  and  $(\mathbf{I} - \frac{\partial \boldsymbol{\xi}(\cdot)}{\partial \mathbf{P}})$  is invertible,  $\boldsymbol{\Pi}$  is a positive definite matrix, and  $\gamma$  is a positive constant. Then PCS kinematic model converges to the desired distal torsion condition.

*Proof.* The proof is given in [32].  $\square$

Note that in the above theorem, we consider  $N$  modes of operation, each of which involves a set of adjacent configurations, and  $\sigma(t) : t \rightarrow \{1 \ \dots \ N\}$  denotes the switching signal that ascertains the linear subsystem associated with the active mode. Here, we need to propose the following definition.

**Definition 3.1.** Adjacent configurations can potentially be made with slight changes in external force and actuators and produce a mode.

**Definition 3.2.** Co-configuration modes contain similar, not adjacent, configurations with an active mode.

#### 4. Stochastic Modeling and Contact Force Estimation

Recalling assumption A6, we consider a quasi-static condition in this work, which means the CTR deforms very slowly, and inertia effects are neglected. In this case, actuator  $\mathbf{q}$  and external force  $\mathbf{F}$ , the inputs shown in Fig. 3, will no longer be constant. Though external force variations depend entirely on environmental conditions, and a precise determination is impossible, especially in an unknown environment, one can expect smooth variation in the force exerted on the robot under quasi-static conditions. Here, we consider the force derivative as white noise and, consequently, express external forces as follows

$$\mathbf{F}(t) = \mathbf{F}_0 + \mathbf{\Omega}_F(\cdot)\mathbf{W}(t) \quad (11)$$

where  $\mathbf{W}(t)$  is a standard Wiener process, and  $\mathbf{F}_0$  denotes the static force that is to be estimated. However, in determining covariance matrix  $\mathbf{\Omega}_F$ , we should take a look back at the PCS kinematic model. When the inputs vary, a deviation from the equilibrium occurs, indicated by distal torsion  $\boldsymbol{\tau}_L$  and restored to balance again by the internal feedback structure. Therefore, one can regard the external force covariance matrix as proportional to distal torsion  $\boldsymbol{\tau}_L$ , which can be given as

$$\mathbf{\Omega}_F(\boldsymbol{\tau}_L) = \omega_F \left| \mathbf{J}_{\boldsymbol{\tau}F\sigma(t)}^T \boldsymbol{\tau}_L \right| \quad (12)$$

in which  $\mathbf{J}_{\boldsymbol{\tau}F\sigma(t)} = \frac{\partial \chi(\cdot)}{\partial \mathbf{F}} + \mathbf{\Gamma} \frac{\partial \xi(\cdot)}{\partial \mathbf{F}}$  and  $\omega_F$  is a positive constant.

**Theorem 2.** *Let CTR be in a quasi-static condition, considering exogenous force  $\mathbf{F}$  as given in (11), and further, assume proximal torsion vector  $\boldsymbol{\tau}_0$  is updated as stated in theorem 1. Then distal torsions are ultimately bounded.*

*Proof.* The proof is given in Appendix B.  $\square$

As a result, we can describe the motion of a loaded CTR with the following state-space stochastic differential equation model.

$$\begin{aligned} d\mathbf{x} &= \mathbf{f}_{\sigma(t)}(\mathbf{x}, \dot{\mathbf{q}})dt + \mathbf{g}_{\sigma(t)}(\mathbf{x}) d\mathbf{W}_t \\ \mathbf{y} &= \mathbf{C}_{\sigma(t)}\mathbf{x} \end{aligned} \quad (13)$$

where  $\mathbf{x} = [\mathbf{F}^T \quad \boldsymbol{\tau}_0^T \quad \mathbf{q}^T]^T$  denotes the state vector, actuator velocity vector  $\dot{\mathbf{q}}$ , and  $\mathbf{y} = [\boldsymbol{\tau}_L^T \quad \mathbf{P}^T]^T$  are the input and output vectors. More, nonlinear functions  $\mathbf{f}_{\sigma(t)}(\mathbf{x}, \dot{\mathbf{q}})$  and  $\mathbf{g}_{\sigma(t)}(\mathbf{x})$ , and constant matrix  $\mathbf{C}_{\sigma(t)}$  are defined as

$$\begin{aligned} \mathbf{f}_{\sigma(t)}(\mathbf{x}, \dot{\mathbf{q}}) &= \begin{bmatrix} 0 \\ -\gamma \mathbf{J}_{\boldsymbol{\tau}\boldsymbol{\tau}\sigma(t)}^T \mathbf{\Pi}^T \chi(\mathbf{x}) \\ \dot{\mathbf{q}} \end{bmatrix} \\ \mathbf{g}_{\sigma(t)}(\mathbf{x}) &= \begin{bmatrix} \omega_F \mathbf{J}_{\boldsymbol{\tau}F\sigma(t)}^T \chi(\mathbf{x}) \\ 0 \\ 0 \end{bmatrix} \\ \mathbf{C}_{\sigma(t)} &= \begin{bmatrix} \mathbf{J}_{\boldsymbol{\tau}F\sigma(t)} & \mathbf{J}_{\boldsymbol{\tau}\boldsymbol{\tau}\sigma(t)} & \mathbf{J}_{\boldsymbol{\tau}q\sigma(t)} \\ \mathbf{J}_{\mathbf{P}F\sigma(t)} & \mathbf{J}_{\mathbf{P}\boldsymbol{\tau}\sigma(t)} & \mathbf{J}_{\mathbf{P}q\sigma(t)} \end{bmatrix} \end{aligned} \quad (14)$$

in which

$$\begin{aligned} \mathbf{J}_{\boldsymbol{\tau}q\sigma(t)} &= \frac{\partial \chi}{\partial \mathbf{q}} + \mathbf{\Gamma} \frac{\partial \xi}{\partial \mathbf{q}}, & \mathbf{J}_{\mathbf{P}F\sigma(t)} &= \left( \mathbf{I} - \frac{\partial \xi}{\partial \mathbf{P}} \right)^{-1} \frac{\partial \xi}{\partial \mathbf{F}} \\ \mathbf{J}_{\mathbf{P}\boldsymbol{\tau}\sigma(t)} &= \left( \mathbf{I} - \frac{\partial \xi}{\partial \mathbf{P}} \right)^{-1} \frac{\partial \xi}{\partial \boldsymbol{\tau}_0}, & \mathbf{J}_{\boldsymbol{\tau}\boldsymbol{\tau}\sigma(t)} &= \left( \mathbf{I} - \frac{\partial \xi}{\partial \mathbf{P}} \right)^{-1} \frac{\partial \xi}{\partial \mathbf{q}} \end{aligned} \quad (15)$$

Now, we derive an estimation of the external forces applied on the corner points included in  $S$  while their spatial positions are known. State vector  $\mathbf{x}$  in (13) is decomposed into unmeasured ( $\mathbf{x}_u$ ) and measured ( $\mathbf{x}_m$ ) sub-vectors.

$$\mathbf{x} = \mathbf{N}_u \mathbf{x}_u + \mathbf{N}_m \mathbf{x}_m, \quad \mathbf{x}_u = [\mathbf{F}^T \quad \boldsymbol{\tau}_0^T]^T, \quad \mathbf{x}_m = \mathbf{q}$$

By linearizing distal torsion function  $\chi(\mathbf{x})$  around operation point  $\sigma(t)$ , we can derive a linear form of  $\mathbf{f}_{\sigma(t)}$  as

$$\mathbf{A}_{\sigma(t)} = \begin{bmatrix} 0 & 0 & 0 \\ \mathbf{Q} \mathbf{J}_{\boldsymbol{\tau}F\sigma(t)} & \mathbf{Q} \mathbf{J}_{\boldsymbol{\tau}\boldsymbol{\tau}\sigma(t)} & \mathbf{Q} \mathbf{J}_{\boldsymbol{\tau}q\sigma(t)} \\ 0 & 0 & 0 \end{bmatrix} \quad (16)$$

where  $\mathbf{Q} = -\gamma \mathbf{J}_{\boldsymbol{\tau}\boldsymbol{\tau}\sigma(t)}^T \mathbf{\Pi}^T$ . The maximum possible deviation of  $\mathbf{f}_{\sigma(t)}$  from its corresponding linearized form  $\mathbf{A}_{\sigma(t)}$  in the operation mode is quantified by

$$\begin{aligned} \left\| \mathbf{f}_{\sigma(t)}(\mathbf{N}_u(\mathbf{x}_u + \boldsymbol{\varepsilon}) + \mathbf{N}_m \mathbf{x}_m, \dot{\mathbf{q}}) - \mathbf{f}_{\sigma(t)}(\mathbf{x}, \dot{\mathbf{q}}) - \mathbf{A}_{\sigma(t)} \begin{bmatrix} \boldsymbol{\varepsilon} \\ 0 \end{bmatrix} \right\| \\ \leq a_2 \left\| \boldsymbol{\varepsilon} \right\| + a_2 \end{aligned} \quad (17)$$

in which  $a_1$  and  $a_2$  are positive constants, and  $\boldsymbol{\varepsilon}$  denotes the variation of  $\mathbf{x}_u$  in operation mode  $\sigma(t)$ . We propose the following full-order observer to estimate the external loads

$$d\hat{\mathbf{x}}_u = \mathbf{N}_u^T \mathbf{f}_{\hat{\sigma}(t)}(\hat{\mathbf{x}}, \dot{\mathbf{q}})dt + \mathbf{L}_{\hat{\sigma}(t)}(\mathbf{y} - \mathbf{C}_{\hat{\sigma}(t)}\hat{\mathbf{x}}) \quad (18)$$

where  $\hat{\mathbf{x}} = [\hat{\mathbf{x}}_u^T \quad \mathbf{x}_m^T]^T$  and we define the estimation error as  $\mathbf{e} = \mathbf{x} - \hat{\mathbf{x}}$ .

**Theorem 3.** *Let the KPCCS system and its observer be in the same mode (i.e.  $\sigma(t) = \hat{\sigma}(t)$ ), switching synchronously with dwell time  $t_D$ . If  $\mathbf{L}_{\sigma(t)}$  is chosen such that  $\text{Re}(\lambda_i(\mathbf{A}_0)) < -\vartheta$  where  $\mathbf{A}_0 = \mathbf{A}_{\sigma(t)} - \mathbf{L}_{\sigma(t)}\mathbf{C}_{\sigma(t)}$  for some  $\vartheta > 0$ , then the estimator (18) will have an almost sure and a mean square exponentially ultimately bounded estimation error if the following condition holds*

$$a_{11} + \frac{\|\mathbf{L}_{\sigma(t)}^T \mathbf{W}\|}{\bar{\lambda}(\mathbf{W})} a_{21} < 0.5 + \frac{\vartheta \underline{\lambda}(\mathbf{W})}{\bar{\lambda}(\mathbf{W})}$$

where  $\mathbf{W}$  is the unique positive-definite solution to

$$(\mathbf{A}_0 + \vartheta \mathbf{I})^T \mathbf{W} + \mathbf{W}(\mathbf{A}_0 + \vartheta \mathbf{I}) = -2\mathbf{I}.$$

*Proof.* The similar proof can be found in [34].  $\square$

**Table 1**  
Physical Quantities For The Experimental Prototype Tubes

	Tube 1	Tube 2
Inner Diameter (mm)	0.385	0.55
Outer Diameter (mm)	0.515	0.76
Curved Length (mm)	125	65
Straight Length (mm)	165	105
Young's Modulus (E) (Gpa)	70	70
Shear Modulus (J) (Gpa)	26.3	26.3
Pre-curvature ( $\kappa^*$ ) ( $m^{-1}$ )	6.46	6.2

Theorem 3 suggests that if the observer correctly detects the system's active mode, it is quite possible to estimate the external forces acting on the robot. However, when the system and observer are in different modes, we first have to detect the actual active mode.

Nevertheless, the configurations' similarity does not mean that they are certainly in the same mode. A common configuration can result from a collection of equivalent and not necessarily close forces. In complicated situations where several point forces act on the backbone, the estimated force set may converge to equivalent force sets rather than the original one applied to the robot.

## 5. Simulation and Experimental Results

To demonstrate the convincing performance of the proposed force estimation approach, we use the exact Cosserat model [35] for simulations and a two-tube prototype for the experimental tests. Tables 1 and 2 list the parameters of two- and three-tube CTRs used in testes.

### 5.1. Evaluation Criteria and Sensing Conditions

To quantify the accuracy of our method and demonstrate its merit, we use position and tangent orientation errors as performance metrics. The true position of the measured points on the backbone is obtained from the Cosserat model [35] in the simulations and the experiments' electromagnetic sensors. Moreover, criterion  $J_e = \|p_{model}(L_1) - p_{data}(L_1)\|/L_1$  is used for the implementation results to evaluate the robot shape accuracy independent of its length during the tests. We investigate different measured points in the simulation analysis to examine the effect of extra sensing points on the accuracy of shape and force estimation and suffice to tip point in the experiments. In all following tests, the estimation algorithm starts with a force-free assumption, and the initial shape of the CTR is described by the piecewise constant curvature (PCC) model.

### 5.2. Simulations Results

The simulations have been performed in three loading situations, including distributed force, constant and variable tip force to investigate the feasibility of the suggested force estimation method. Since the Cosserat model's implementation is time-consuming, we executed it with a low sampling frequency on the simulation

**Table 2**  
The CTR parameters used for simulation

	Tube 1	Tube 2	Tube 3
Inner Diameter (mm)	0.385	0.55	0.8
Outer Diameter (mm)	0.515	0.76	0.9
Curved Length (mm)	100	50	50
Straight Length (mm)	165	105	85
Young's Modulus (E) (Gpa)	70	70	70
Shear Modulus (G) (Gpa)	26.31	26.31	26.31
Pre-curvature ( $\kappa^*$ ) ( $m^{-1}$ )	6.46	6.2	5

path. We then interpolated the remaining missing observations (30 samples between two consecutive original samples) to achieve adequate time resolution for ground truth data. The switching time in all simulations is considered 40 times longer than the sampling rate. During the simulation, actuator vector  $\mathbf{q} = [\mathbf{q}_\alpha^T \ \mathbf{q}_\beta^T]^T$  changes from  $[\pi/4 \ 0 \ 0 \ 0.2 \ 0.12 \ 0.06]^T$  to  $[\pi/3 \ \pi/5 \ -\pi/3 \ 0.21 \ 0.14 \ 0.07]^T$  at a constant slope, where  $\mathbf{q}_\alpha$  and  $\mathbf{q}_\beta$  denote the tubes' base rotation and exterior length vectors.

We compare the ground truth data obtained from the Cosserat model with the PCC model results, in which external loads are neglected, to demonstrate the effect of the applied forces on the robot shape. The spatial position error of the points along the backbone under the different loading conditions is given in Fig. 4. The results show the tip position average errors are about 25 – 35% of the robot length in the tip-point loading tests (Fig. 4(a,b)) and 10% in the distributed loading test (Fig. 4(c)). The performance of the estimation method has been investigated from two aspects. One is the estimated shape error, and the other is the estimated force convergence to the true value applied to the backbone. Fig. 5 and Fig. 6 show the force estimation while the CTR experiences a constant and variable tip force, respectively, and the tip point's position is assumed to be known in both cases. The dashed lines mark the actual values of the applied forces in these figures. Moreover, Fig. 7 illustrates the norm of the spatial position error during the simulations performed under the two mentioned tip-force conditions. By looking at Fig. 7(a,b) and comparing it to Fig. 4(a,b), one can see the effect of the force estimation algorithm on reducing the robot shape error. This reduction in error occurs more rapidly than the convergence of the estimated forces into their actual values. This means reaching and switching among modes with configurations close to the actual one. Fig. 8 shows the distributed force acting on the backbone in the last simulation test, and the corresponding discrete one we expect to estimate. As demonstrated in Fig. 9(a) the estimation algorithm decreases the CTR configuration error to an acceptable level (about 2.5% of the length on average). Nonetheless, the estimated force does not converge to the desired value. This may be because more modes can create configurations close to the robot's actual shape when multiple point forces apply on it. This is also true in the case of

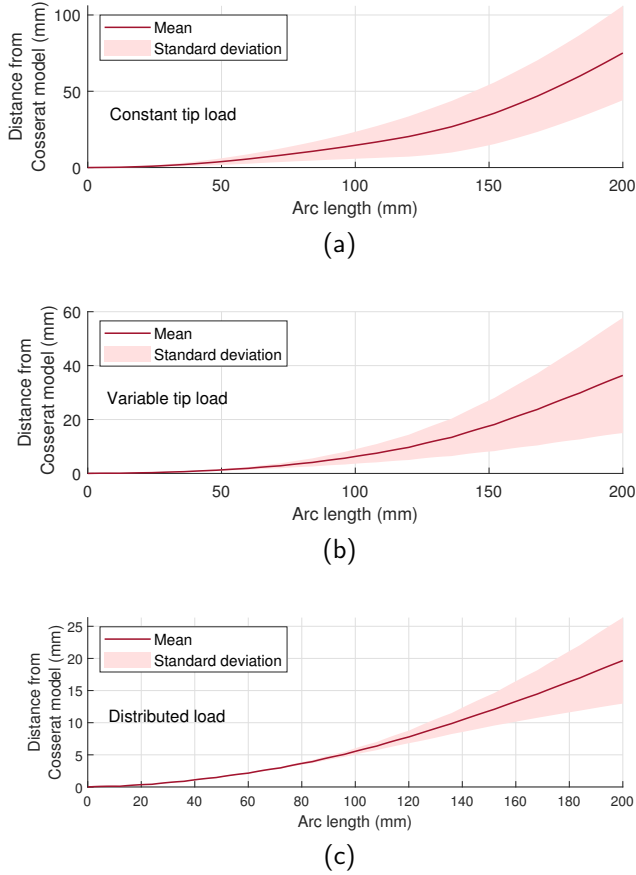


**Figure 4:** The Euclidean distance between the corresponding points of the PCC and Cosserat models along the CTR. The significance of the external loads applied in the simulations on deforming the CTR and the demand for force estimation is demonstrated. We used the norm of the position error from comparing the PCC model considering no external load with the exact Cosserat model under an external a) constant tip force, b) variable tip force, and c) distributed force. The mean and standard deviation of the error norms are indicated along the backbone for different configurations during the simulation time.

discretizing force distribution with three point forces (Fig. 9(b)). Comparing Fig. 9(a) and (b) shows the robot shape estimation converges slower in the three-point examination.

### 5.3. Robot Prototype and Measurement Methods

As shown in Fig. 10, the experimental platform involves a concentric-tube robot prototype and an Aurora electromagnetic tracking system (EMTS) manufactured by Northern Digital Inc. The CTR comprises two NiTi tubes, the physical properties of which are listed in Table 1. All tubes are of proximal straight lengths on the actuation unit and are followed by a curved section. They are translated and rotated independently. So, the actuator vector  $\mathbf{q}_a = [\alpha_1 \ \alpha_2 \ \beta_1 \ \beta_2]$ , in which  $\alpha_1, \alpha_2 \in [-\pi \ \pi]$ ,  $\beta_1 \in [0.165 \ 0.225]$  and  $\beta_2 \in [0.105 \ 0.135]$ , defines the achievable configuration space of the CTR in free space. The initial configuration's outward length of inner and outer

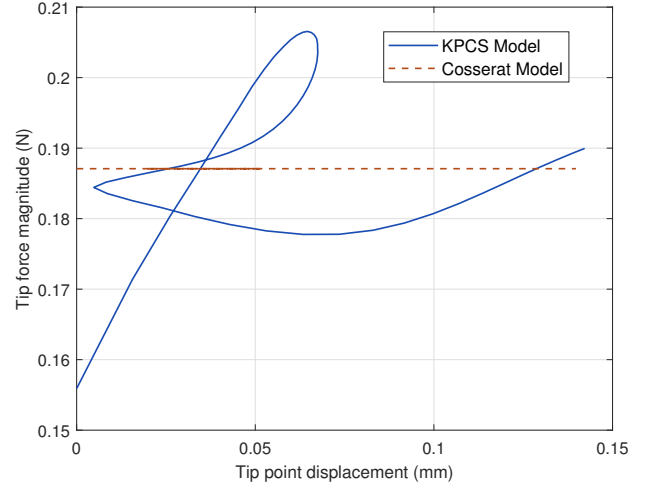


**Figure 5:** The distal point force-displacement diagram in the constant tip loading condition for the Cosserat and KPCS models

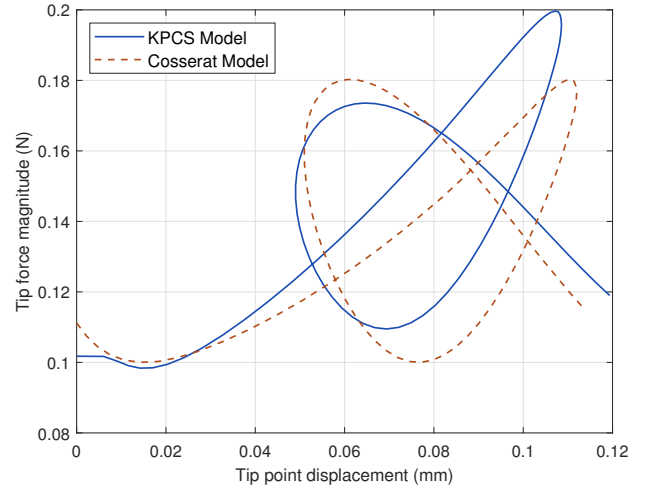


**Figure 6:** The distal point force-displacement diagram in the variable tip loading condition for the Cosserat and KPCS models

tubes are 0.095 and 0.04, respectively. In our experiments, the CTR took four different paths in the actuator space that all started at point  $\mathbf{q}_{aI} = [0 \ 0 \ 0.195 \ 0.115]^T$ . They ended at point  $\mathbf{q}_{aE} = [\alpha_{1e} \ \alpha_{2e} \ \beta_{1e} \ \beta_{2e}]^T$  and were sampled at a rate of  $\delta \mathbf{q}_a = [\delta \alpha_1 \ \delta \alpha_2 \ \delta \beta_1 \ \delta \beta_2]^T$  (see Table 3). We examined the estimation performance while the CTR moved along these different paths. As specified in Fig. 10, the EMT system determines the robot's base-point and end-point positions. The dimension of the prototype easily allows keeping its workspace within measurement volume (a cube with edges of length about 50cm). Sensors are small coils in which weak currents are induced by the varying electromagnetic field produced by the field generator. As depicted in Fig. 10, we used the Aurora 5DOF Flex Tube at

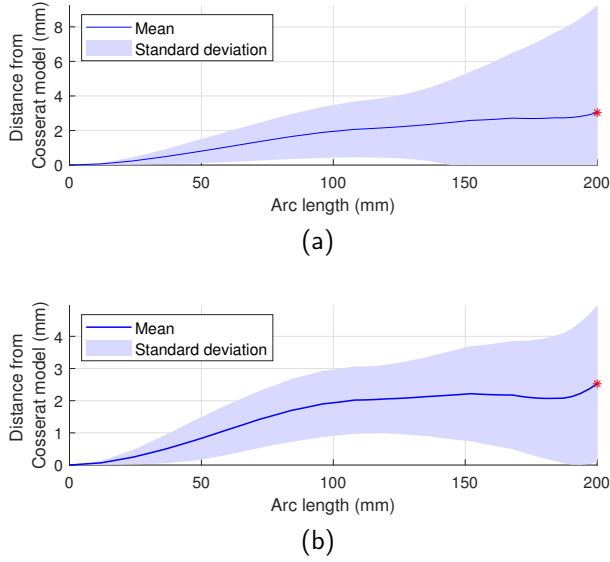


**Figure 7:** The Euclidean distance between the corresponding points of curves obtained from the KPCS (with force estimation) and Cosserat models, along the backbone for different configurations under constant (a) and variable (b) tip force. The position of the point depicted by the red star is assumed to be known.

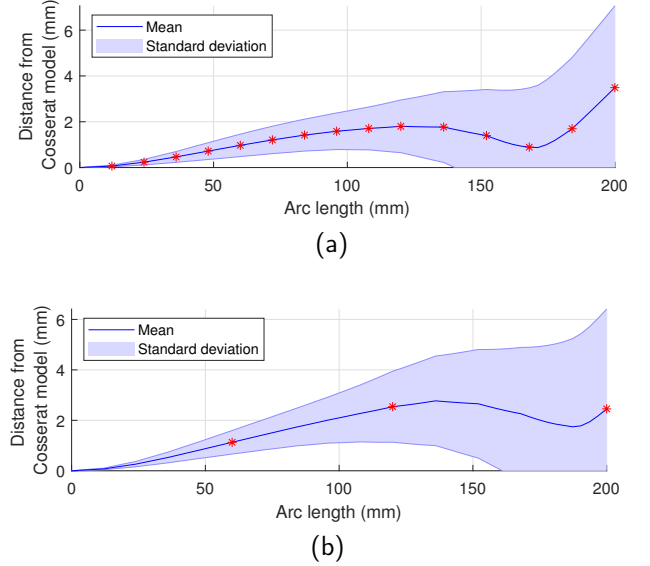


**Figure 9:** The Euclidean distance between the corresponding points of curves obtained from the KPCS (with force estimation) and Cosserat models, along the backbone for different configurations under external distributed force. The position of the arc-lengths indicated by stars is assumed to be known.

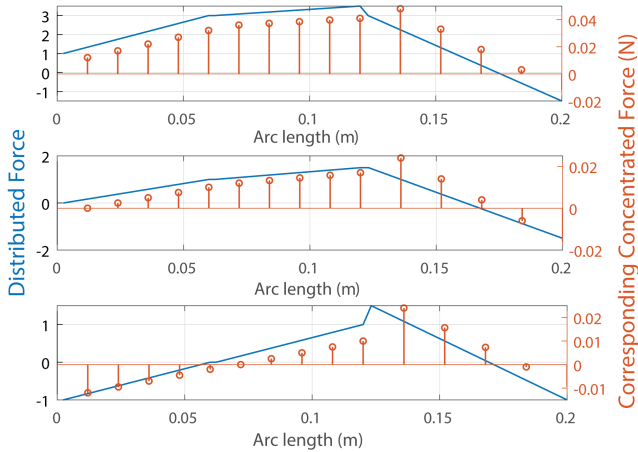


**Figure 8:** The distributed force used in the simulation test and its corresponding concentrated forces in the KPCS model that is expected to be estimated.

the base because it shows more robustness against the disturbance caused by some metallic components of the actuation unit. We likewise used the Aurora Micro 6DOF at the end-point, the most miniature 6DOF sensor offered by NDI. The system control unit (SCU) sends the position and orientation data to the host computer through a USB connection.

#### 5.4. Experimental Results

This section addresses the evaluation of the estimation method implemented on a two-tube CTR. As shown in Fig. 10, the experiments were performed with a weight hung from the tip and repeated with different masses. The motion

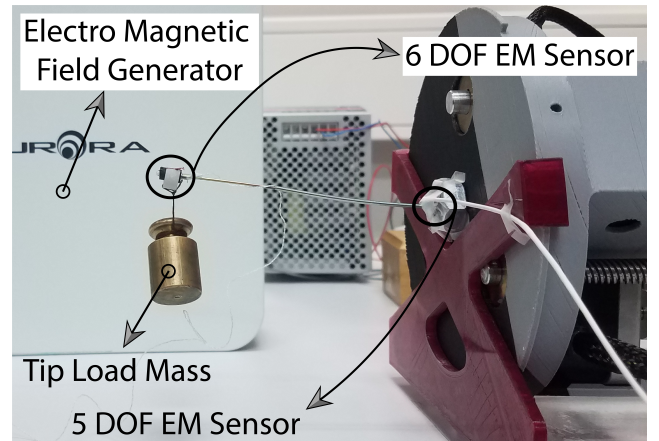


**Figure 10:** Experimental setup consisting of a concentric tube robot, an electromagnetic tracker and two coils mounted at the base and tip of the robot which are used to measure the position.

of the CTR makes a slight pendulum-like swinging movement to the hung weight and consequently changes the direction of the applied force echoes in distal torsions. Moreover, some neglected details in the model, like clearance and friction among the tubes or between the outermost tube and the hole drilled in the base plate, and manufacturing errors such as tolerance of pre-curvatures and length, can be seen as disturbance forces that deform the robot shape.

We consider the CTR end-point position and orientation information to evaluate the robot's shape accuracy (see Fig. 11). Fig. 12 and Fig. 13 demonstrate the position and Euler angle error of the end-effector of the CTR. They represent the performance of the proposed approach in estimating the

**Table 3**  
Paths of the CTR in the Actuator Space

	Translation (mm)				Rotation (deg)			
	$\beta_{1e}$	$\beta_{2e}$	$\delta\beta_1$	$\delta\beta_2$	$\alpha_{1E}$	$\alpha_{2E}$	$\delta\alpha_1$	$\delta\alpha_2$
1	165	110	0.2	0.2	180	45	0.5	0.15
2	165	105	0.2	0.1	180	0	0.5	0
3	175	130	0.6	-0.3	90	-90	0.8	-0.8
4	175	130	0.08	-0.1	-270	90	-0.8	0.4

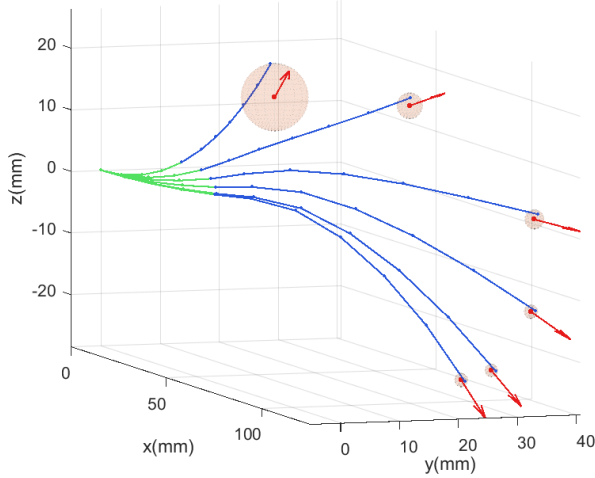


**Figure 11:** The configurations of the two-tube CTR carrying a 20gr weight and on the path defined in Table 3. The KPCS model with external force estimation describes it. The radius of the red spheres indicates reduced tip position error due to force estimation. The arrows show the measured direction of the endpoint

CTR shape while it was traversing path 1 in actuator space and carrying a 20 gr weight. Since, at the starting point, the robot and the force acting on it both were on the x-z plane, the position error y was initially zero, and the Euler angle error was only for the y component.

Furthermore, along this path, the estimated force on the robot tip is shown in Fig 14. As was expected, the tip force in the x-direction eventually attained  $-0.2N$  caused due to the hung weight. It seems the unexpected forces estimated in the y and z directions compensate for some of the uncertainties in the PCS kinematic model.

To investigate the effect of force estimation on the uncertainty and shape error reduction, we have repeated the experiment with the actual value of the weight and without the estimation algorithm. In Fig. 15, we compared the end-point position error in these two cases while the CTR moved along the four paths given in Table 3. Moreover, the first 15 samples of the data obtained from each path are omitted to lessen the transition effect on the results and provide a more careful examination of the estimated force. It can be seen the force estimation reduced the average end-point error to less than half, confirming its effect on the uncertainty reduction.

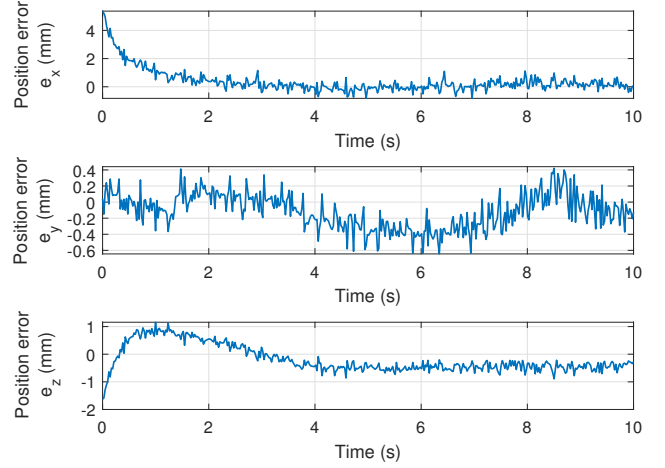


**Figure 12:** The end-effector position error of the two-tube CTR carrying a 20gr weight. The actuators take the first path in Table 3. The CTR is described by the KPCS model with external force estimation.

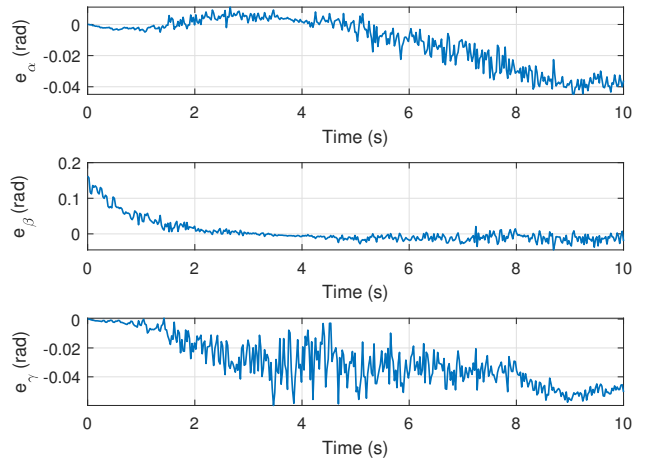


**Figure 13:** The Euler angle error of the two-tube CTR end-effector carrying a 20gr weight and its actuators take the first path in Table 3. The KPCS model with external force estimation describes the CTR.

## 5.5. Discussion

The inherent flexibility of robots makes the robot not only a function of its actuators but also external forces. Therefore, the unpredictable nature of external forces complicates analyzing the robot shape and motion doubtlessly. We have presented in this work a stochastic model for the external force applied on CTRs, assuming the quasi-static constraint. We considered the external force covariance matrix dependent on the distal torsion because its deviation from the equilibrium condition means a change in the inputs and potentially an unexpected change in external force. Such a stochastic external force model transforms the robotic kineto-static model into a stochastic differential equation. A



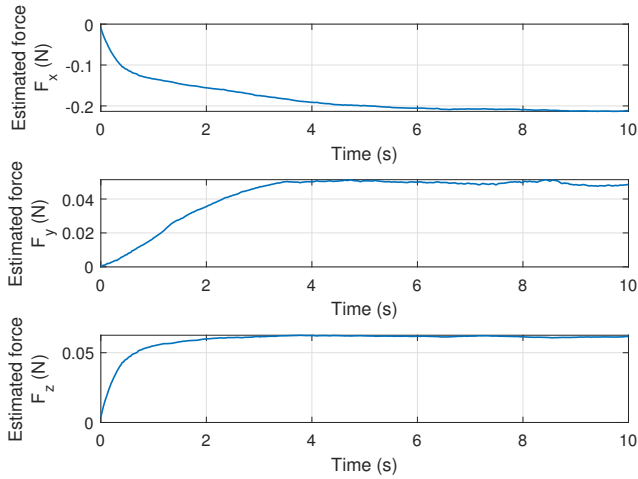


**Figure 14:** The estimated force of the two-tube CTR carrying a 20gr weight while the actuators move on the first path given in Table 3. The force in the x direction is correctly estimated but doesn't fit the expectations in the y and z direction. The reason is to compensate for some of the prototype's uncertainties and get a better shape estimation, as shown in Fig 15.

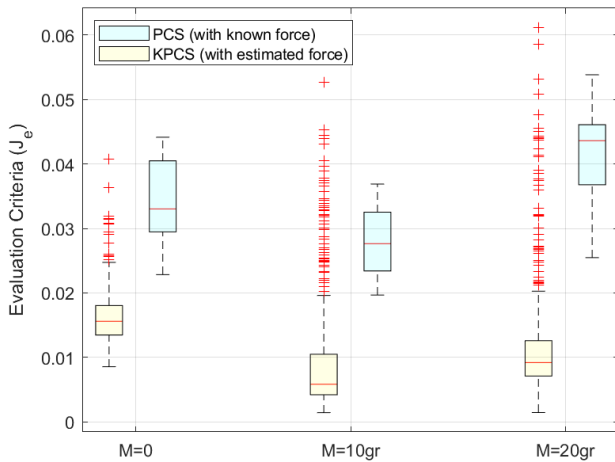


**Figure 15:** The comparison of evaluation criteria  $J_e$  (normalized tip error) when 1) the external force is considered known, and 2) external force is unknown and estimated. Since it initiates in an unloaded condition, the estimation algorithm causes a wider range of errors, increasing with the load. However, the estimation provides a significantly lower mean error for all loading conditions.

stochastic observer has been proposed to estimate the forces using the position data of the distinct points on the backbone.

The issue is that for a CTR, there is not necessarily a one-to-one correspondence between the configuration set and the applied force set. So, one can consider a subset of forces called equivalent forces that may be entirely dissimilar but exert a shared influence on the robot shape and create identical deformations. Consequently, the observer may converge

to one of those equivalent forces corresponding to the co-configuration modes. As was depicted in Fig. 5 and Fig. 6, the convergence of estimated force to the actual value occurred in the tip-concentrated force cases. However, it failed in the distributed one, where we expected it to converge into the corresponding discretized force (Fig. 8). One can only be sure that the observer has reached one of the co-configuration modes. The computation time of the proposed force estimation method depends on the number of points measured. The average time for each sample is about 3.8 ms for tip loading and 6.2 and 20 ms for distributed loads with three and fifteen measuring points, respectively. A relatively long dwell time guarantees the stability of the observer. However, one can expect to achieve less conservative results and faster convergence using state-based switching methods. The implementation results show differences between the estimated external force and the actual force applied to the robot, especially in the y- and z-axes (Fig. 14). These differences are mainly due to the uncertainties of the robot model. To show this matter, we compare the robot shape error (normalized tip error) in two assumptions of the known applied force (a known hung weight) and the unknown one, obtained from estimating based on position data (Fig. 15).

Overall, the proposed method has successfully estimated the robot's shape (Fig. 7 and Fig. 9) and has efficiently assessed the applied force in the tip-point loading case (Fig. 5 and Fig. 6). However, estimating the distributed force or multiple point forces solely through the backbone position data was not satisfactory. In this case, the estimation algorithm can only guarantee convergence to the set of forces equivalent to the one applied to the robot.

## 6. Conclusion

This study presented a model-based force estimation method for CTRs using position sensing techniques. It helps the robot sense the applied force while navigating through the patient's anatomy and perform planned maneuvers successfully in a confined space. Following the previously developed PCS kinematics [32], we proposed a kineto-static model using the Wiener process to characterize unpredictable external forces. The resultant stochastic switched system describes the behavior of CTRs when they move slowly in unknown constraint environments. A linear stochastic observer has been proposed for each system mode to estimate external force by measuring distinct points' position data along the backbone. The findings confirm that the estimated forces can considerably reduce the position error along CTRs (see Fig. 7, Fig. 9 and Fig. 12). However, when the shape error converges to zero, the observer operates not necessarily in the active mode but in the co-configuration ones. Thus, the estimated force tends to the actual value only in simple loading conditions, such as tip-concentrated force. In more complex situations, such as distributed force, it converges to the equivalent forces associated with the configuration. The implementation results also show the capa-

bility of the proposed method in compensating the uncertainties to achieve a more accurate shape approximation of the CTR prototype. Further studies should investigate the development of the method to non-positional data (such as measuring strains) to estimate the external moments exerted on CTRs, or mode detection of the switched system needed to escape the trap of equivalent forces. In addition, we need to examine whether merely knowing the robot's shape, estimating the equivalent forces rather than the real one in the distributed load provides secure control of CTRs in these situations.

## A. Proof of Equation (6)

Discretizing the x-y curvatures and keeping the torsion continuous along the CTR, the angular vector in the stressed an unstressed conditions can be given as

$$\begin{aligned} \bar{u}_{i,j} &= [-\kappa_j \sin(\phi_j) \quad \kappa_j \cos(\phi_j) \quad \tau_i(s)]^T \\ \bar{u}_{i,j}^* &= [-\kappa_{i,j}^* \sin(\theta_i(s)) \quad \kappa_{i,j}^* \cos(\theta_i(s)) \quad \tau_{e_i}^*(s)]^T \end{aligned} \quad (19)$$

where  $\tau_{e_i}^*(s)$  is the torsion produced from pre-torsion and applied external load. So, the stored strain energy of the  $i$ th tube can be given in

$$J = \frac{1}{2} \int_{-\beta_i}^{L_i} (\bar{u}_{i,j} - \bar{u}_{i,j}^*)^T K_i (\bar{u}_{i,j} - \bar{u}_{i,j}^*) ds \quad (20)$$

where  $K_i$  is stiffness matrix defined as

$$K_i = \text{diag}(E_i I_i, E_i I_i, G_i J_i) \quad (21)$$

From (19), (20) and (21), we can rewrite energy function  $J$  as

$$J = \frac{1}{2} \int_{-\beta_i}^{L_i} f(\theta_i(s), \tau_i(s)) ds \quad (22)$$

where

$$\begin{aligned} f(\theta_i(s), \tau_i(s)) &= E_i I_i (\kappa_j^2 + \kappa_{i,j}^{*2} - \kappa_j \kappa_{i,j}^* \cos(\phi_j - \theta_i(s))) \\ &\quad + G_i J_i (\tau_i(s) - \tau_{e_i}^*(s))^2 \end{aligned}$$

Suppose that  $\theta_i(s) = \bar{\theta}_i(s) + \epsilon \tilde{\theta}_i(s)$  is perturbed from equilibrium value  $\bar{\theta}_i(s)$ , and  $\epsilon$  is small. So, knowing that  $\tau_i(s) = d\theta(s)/ds$ , we find the minimum energy after small perturbation by

$$\frac{dJ}{d\epsilon} = \frac{1}{2} \int_{-\beta_i}^{L_i} \frac{\partial f(\cdot)}{\partial \tau_i(s)} \tilde{\tau}_i(s) + \frac{\partial f(\cdot)}{\partial \theta_i(s)} \tilde{\theta}_i(s) ds \quad (23)$$

Using integration by parts on the first term, we have

$$\frac{dJ}{d\epsilon} = \frac{1}{2} \int_{-\beta_i}^{L_i} \left( \frac{\partial f(\cdot)}{\partial \theta_i(s)} - \frac{d}{ds} \frac{\partial f(\cdot)}{\partial \tau_i(s)} \right) \tilde{\theta}_i(s) ds + \tilde{\theta}_i(s) \frac{\partial f(\cdot)}{\partial \tau_i(s)} \Big|_{-\beta_i}^{L_i}$$

By imposing the following boundary conditions

$$\tilde{\theta}_i(-\beta_i) = 0, \quad \frac{\partial f(\cdot)}{\partial \tau_i(s)} \Big|_{s=L_i} = 0 \quad (24)$$

The minimum energy found by

$$\frac{\partial f(\cdot)}{\partial \theta_i(s)} - \frac{d}{ds} \frac{\partial f(\cdot)}{\partial \tau_i(s)} = 0 \quad (25)$$

So, from (25) and by discretizing torsion along the backbone, one can get (6).

## B. Proof of Theorem 2

*Proof.* Let  $V(\tau_L) = \frac{1}{2} \tau_L^T \Pi \tau_L$  be a Lyapunov function meeting the CTR model validity in static conditions. Differentiating from (9), we have

$$d\tau_L = J_{\tau F_{\sigma(t)}} dF + J_{\tau q_{\sigma(t)}} dq + J_{\tau \tau_{\sigma(t)}} d\tau_0 \quad (26)$$

in which

$$\begin{aligned} J_{\tau \tau_{\sigma(t)}} &= \frac{\partial \chi(x)}{\partial \tau_0} + \Gamma \frac{\partial \xi(x)}{\partial \tau_0}, \quad J_{\tau F_{\sigma(t)}} = \frac{\partial \chi(x)}{\partial F} + \Gamma \frac{\partial \xi(x)}{\partial F} \\ J_{\tau q_{\sigma(t)}} &= \frac{\partial \chi(x)}{\partial q} + \Gamma \frac{\partial \xi(x)}{\partial q} \end{aligned}$$

and  $\Gamma = \frac{\partial \chi(x)}{\partial P} (I - \frac{\partial \xi(x)}{\partial P})^{-1}$ . Substituting  $\dot{\tau}_0 = -\gamma J_{\tau \tau_{\sigma(t)}}^T \Pi^T \tau_L$  and the t-derivative of (11), into (26) gives

$$d\tau_L = f_{\tau}(\tau_L, \dot{q}) dt + \Omega_F(\tau_L) dW \quad (27)$$

where

$$f_{\tau}(\tau_L, \dot{q}) = (-\gamma J_{\tau \tau_{\sigma(t)}} J_{\tau \tau_{\sigma(t)}}^T \Pi^T \tau_L + J_{\tau q_{\sigma(t)}} \dot{q}) \quad (28)$$

We define the differential operator  $\mathcal{L}$  as follows

$$\mathcal{L}V = \frac{\partial V}{\partial \tau_L} f_{\tau}(\tau_L, \dot{q}) + \frac{1}{2} \text{Tr} \{ \Omega_F(\tau_L)^T \frac{\partial^2 V}{\partial x^2} \Omega_F(\tau_L) \} \quad (29)$$

So, from (12) and (28)

$$\begin{aligned} \mathcal{L}V &= -\tau_L^T \Pi (\gamma J_{\tau \tau_{\sigma(t)}} J_{\tau \tau_{\sigma(t)}}^T \Pi^T \tau_L + J_{\tau q_{\sigma(t)}} \dot{q}) \\ &\quad + \frac{1}{2} \omega_F^2 \text{Tr} \{ \tau_L^T J_{\tau F_{\sigma(t)}} \Pi J_{\tau F_{\sigma(t)}}^T \tau_L \} \end{aligned} \quad (30)$$

Assuming  $\Pi = \Pi^T \Pi'$  and  $\Theta_1 + \Theta_2 < 1$  in which  $\Theta_1$  and  $\Theta_2$  are positive scalars, yields

$$\begin{aligned} \mathcal{L}V &\leq -\gamma(1 - \Theta_1 - \Theta_2) \tau_L^T \Pi J_{\tau \tau_{\sigma(t)}} J_{\tau \tau_{\sigma(t)}}^T \Pi^T \tau_L \\ &\quad - \gamma \Theta_1 \underline{\lambda} (\Pi J_{\tau \tau_{\sigma(t)}} J_{\tau \tau_{\sigma(t)}}^T \Pi^T) \|\tau_L\|^2 \\ &\quad - \gamma \Theta_2 \underline{\lambda} (\Pi J_{\tau \tau_{\sigma(t)}} J_{\tau \tau_{\sigma(t)}}^T \Pi^T) \|\tau_L\|^2 \\ &\quad + |\bar{\lambda} (\Pi J_{\tau q_{\sigma(t)}})| \|\tau_L\| \dot{q} + \omega_F^2 \|\Pi' J_{\tau F_{\sigma(t)}}\|_F^2 \|\tau_L\|^2 \end{aligned} \quad (31)$$

Then for  $\gamma > \frac{\omega_F^2 \|\Pi' J_{\tau F_{\sigma(t)}}\|_F^2}{\Theta_2 \underline{\lambda} (\Pi J_{\tau \tau_{\sigma(t)}} J_{\tau \tau_{\sigma(t)}}^T \Pi^T)}$

$$\begin{aligned} \mathcal{L}V &\leq -\gamma(1 - \Theta_1 - \Theta_2) \tau_L^T \Pi J_{\tau \tau_{\sigma(t)}} J_{\tau \tau_{\sigma(t)}}^T \Pi^T \tau_L \\ &\quad \forall \dot{q} \leq \rho \|\tau_L\| \end{aligned} \quad (32)$$

where

$$\rho = \frac{\gamma \Theta_1 \underline{\lambda} (\Pi J_{\tau \tau_{\sigma(t)}} J_{\tau \tau_{\sigma(t)}}^T \Pi^T)}{|\bar{\lambda} (\Pi J_{\tau F_{\sigma(t)}})|}$$

Since all individual subsystems are stochastic asymptotically stable for  $V(\tau_L)$ , there is a dwell-time  $t_D$  that allows the transient effect to dissipate after each switch.  $\square$

## References

- [1] Zheng Li, Liao Wu, Hongliang Ren, and Haoyong Yu. Kinematic comparison of surgical tendon-driven manipulators and concentric tube manipulators. *Mechanism and machine theory*, 107:148–165, 2017.
- [2] Margaret F Rox, Dominick S Ropella, Richard J Hendrick, Evan Blum, Robert P Naftel, Hansen C Bow, S Duke Herrell, Kyle D Weaver, Lola B Chambless, and Robert J Webster III. Mechatronic design of a two-arm concentric tube robot system for rigid neuroendoscopy. *IEEE/ASME Transactions on Mechatronics*, 25(3):1432–1443, 2020.
- [3] Cedric Girerd, Patrick Rougeot, Olivier Lehmann, Laurent Tavernier, Jerome Szewczyk, Kanty Rabenorosoa, et al. A hybrid concentric tube robot for cholesteatoma laser surgery. *IEEE Robotics and Automation Letters*, 2021.
- [4] Quentin Peyron, Kanty Rabenorosoa, Nicolas Andreff, and Pierre Renaud. A numerical framework for the stability and cardinality analysis of concentric tube robots: Introduction and application to the follow-the-leader deployment. *Mechanism and Machine Theory*, 132:176–192, 2019.
- [5] Nikolay V Vasilyev, Andrew H Gosline, Arun Veeramani, Ming Ting Wu, Gregory P Schmitz, Richard T Chen, Veaceslav Arabagi, Pedro J Del Nido, and Pierre E Dupont. Tissue removal inside the beating heart using a robotically delivered metal mems tool. *The International Journal of Robotics Research*, 34(2):236–247, 2015. doi: 10.1177/0278364914543671.
- [6] Jessica Burgner, D Caleb Rucker, Hunter B Gilbert, Philip J Swaney, Paul T Russell, Kyle D Weaver, and Robert J Webster. A telerobotic system for transnasal surgery. *IEEE/ASME Transactions on Mechatronics*, 19(3):996–1006, 2013. doi: 10.1109/TMECH.2013.2265804.
- [7] Hessa Alfalahi, Federico Renda, and Cesare Stefanini. Concentric tube robots for minimally invasive surgery: Current applications and future opportunities. *IEEE Transactions on Medical Robotics and Bionics*, 2(3):410–424, 2020.
- [8] Zisos Mitros, SM Hadi Sadati, Ross Henry, Lyndon Da Cruz, and Christos Bergeles. From theoretical work to clinical translation: Progress in concentric tube robots. *Annual Review of Control, Robotics, and Autonomous Systems*, 5, 2021.
- [9] Hunter B Gilbert, D Caleb Rucker, and Robert J Webster III. Concentric tube robots: The state of the art and future directions. In *Robotics Research*, pages 253–269. Springer, 2016.
- [10] Heiko Donat, Sven Lilge, Jessica Burgner-Kahrs, and Jochen J Steil. Estimating tip contact forces for concentric tube continuum robots based on backbone deflection. *IEEE Transactions on Medical Robotics and Bionics*, 2(4):619–630, 2020.
- [11] Kai Xu and Nabil Simaan. Intrinsic wrench estimation and its performance index for multisegment continuum robots. *IEEE Transactions on Robotics*, 26(3):555–561, 2010.
- [12] Kai Xu and Nabil Simaan. An investigation of the intrinsic force sensing capabilities of continuum robots. *IEEE Transactions on Robotics*, 24(3):576–587, 2008.
- [13] Chaoyang Shi, Xiongbiao Luo, Peng Qi, Tianliang Li, Shuang Song, Zoran Najdovski, Toshio Fukuda, and Hongliang Ren. Shape sensing techniques for continuum robots in minimally invasive surgery: A survey. *IEEE Transactions on Biomedical Engineering*, 64(8):1665–1678, 2016.
- [14] Alfred M Franz, Tamas Haidegger, Wolfgang Birkfellner, Kevin Cleary, Terry M Peters, and Lena Maier-Hein. Electromagnetic tracking in medicine—a review of technology, validation, and applications. *IEEE transactions on medical imaging*, 33(8):1702–1725, 2014.
- [15] Seok Chang Ryu and Pierre E Dupont. Fbg-based shape sensing tubes for continuum robots. In *2014 IEEE International Conference on Robotics and Automation (ICRA)*, pages 3531–3537. IEEE, 2014.
- [16] Fouzia Khan, Alper Denasi, David Barrera, Javier Madrigal, Salvador Sales, and Sarthak Misra. Multi-core optical fibers with bragg gratings as shape sensor for flexible medical instruments. *IEEE sensors journal*, 19(14):5878–5884, 2019.
- [17] Shahir Hasanzadeh and Farrokh Janabi-Sharifi. Model-based force estimation for intracardiac catheters. *IEEE/ASME Transactions on Mechatronics*, 21(1):154–162, 2015.
- [18] Mahta Khoshnam, Allan C Skanes, and Rajni V Patel. Modeling and estimation of tip contact force for steerable ablation catheters. *IEEE Transactions on Biomedical Engineering*, 62(5):1404–1415, 2015.
- [19] Junghwan Back, Thomas Manwell, Rashed Karim, Kawal Rhode, Kaspar Althoefer, and Hongbin Liu. Catheter contact force estimation from shape detection using a real-time cosserat rod model. In *2015 IEEE/RSJ International Conference on Intelligent Robots and Systems (IROS)*, pages 2037–2042. IEEE, 2015.
- [20] D Caleb Rucker and Robert J Webster. Deflection-based force sensing for continuum robots: A probabilistic approach. In *2011 IEEE/RSJ International Conference on Intelligent Robots and Systems*, pages 3764–3769. IEEE, 2011.
- [21] Venkatasubramanian Kalpathy Venkiteswaran, Jakub Sikorski, and Sarthak Misra. Shape and contact force estimation of continuum manipulators using pseudo rigid body models. *Mechanism and machine theory*, 139:34–45, 2019.
- [22] Alessandro Vandini, Christos Bergeles, Ben Glocker, Petros Giataganas, and Guang-Zhong Yang. Unified tracking and shape estimation for concentric tube robots. *IEEE Transactions on Robotics*, 33(4):901–915, 2017.
- [23] Qiao Qiao, Gianni Borghesan, Joris De Schutter, and Emmanuel Vander Poorten. Force from shape—estimating the location and magnitude of the external force on flexible instruments. *IEEE Transactions on Robotics*, 37(5):1826–1833, 2021.
- [24] Fan Feng, Wuzhou Hong, and Le Xie. A learning-based tip contact force estimation method for tendon-driven continuum manipulator. *Scientific Reports*, 11(1):1–11, 2021.
- [25] Mohsen Khadem, John O’Neill, Zisos Mitros, Lyndon Da Cruz, and Christos Bergeles. Autonomous steering of concentric tube robots for enhanced force/velocity manipulability. In *2019 IEEE/RSJ International Conference on Intelligent Robots and Systems (IROS)*, pages 2197–2204. IEEE, 2019.
- [26] Mohsen Khadem, John O’Neill, Zisos Mitros, Lyndon Da Cruz, and Christos Bergeles. Autonomous steering of concentric tube robots via nonlinear model predictive control. *IEEE Transactions on Robotics*, 36(5):1595–1602, 2020.
- [27] Cedric Girerd, Andrey V Kudryavtsev, Patrick Rougeot, Pierre Renaud, Kanty Rabenorosoa, and Brahim Tamadazte. Slam-based follow-the-leader deployment of concentric tube robots. *IEEE Robotics and Automation Letters*, 5(2):548–555, 2020.
- [28] Ahmad Abu Alqumsan, Suiyang Khoo, and Michael Norton. Robust control of continuum robots using cosserat rod theory. *Mechanism and Machine Theory*, 131:48–61, 2019.
- [29] Balint Thamo, Kev Dhaliwal, and Mohsen Khadem. Rapid solution of cosserat rod equations via a nonlinear partial observer.
- [30] Federico Renda, Frédéric Boyer, Jorge Dias, and Lakmal Seneviratne. Discrete cosserat approach for multisection soft manipulator dynamics. *IEEE Transactions on Robotics*, 34(6):1518–1533, 2018.
- [31] Federico Renda, Vito Cacucciolo, Jorge Dias, and Lakmal Seneviratne. Discrete cosserat approach for soft robot dynamics: A new piece-wise constant strain model with torsion and shears. In *2016 IEEE/RSJ International Conference on Intelligent Robots and Systems (IROS)*, pages 5495–5502. IEEE, 2016.
- [32] Mahdi Pourafzal, Heidar Ali Talebi, and Kanty Rabenorosoa. Piece-wise constant strain kinematic model of externally loaded concentric tube robots. *Mechatronics*, 74:102502, 2021.
- [33] D Caleb Rucker, Robert J Webster III, Gregory S Chirikjian, and Noah J Cowan. Equilibrium conformations of concentric-tube continuum robots. *The International journal of robotics research*, 29(10):1263–1280, 2010.
- [34] E Yaz and Asad Azemi. Observer design for discrete and continuous non-linear stochastic systems. *International Journal of systems science*, 24(12):2289–2302, 1993.
- [35] D Caleb Rucker, Bryan A Jones, and Robert J Webster III. A geometrically exact model for externally loaded concentric-tube continuum

robots. *IEEE Transactions on Robotics*, 26(5):769–780, 2010.



Mahdi Pourafzal received the B.Sc. degree from Shahed University, Tehran, Iran, in 2010, and the M.Sc. degree from K. N. Toosi University of Technology, Tehran, Iran, in 2013, both in electrical engineering. He is currently pursuing the Ph.D. degree in electrical engineering at Amirkabir University of Technology, Tehran, Iran. His research interests include medical robotics, continuum robotics and control of nonlinear systems.



Heidar A. Talebi received the B.Sc. degree in electrical engineering from Ferdowsi University, Mashhad, Iran, in 1988, the M.Sc. degree in electrical engineering from Tarbiat Modarres University, Tehran, Iran, in 1991, and the Ph.D. degree in electrical engineering from Concordia University, Montreal, QC, Canada, in 1997. He was a Postdoctoral Fellow and a Research Fellow with Concordia University and the University of Western Ontario. In 1999, he joined the Amirkabir University of Technology, Tehran, where he is currently a Professor and the Chair of the Department of Electrical Engineering. His research interests include control, robotics, medical robotics, fault diagnosis and recovery, intelligent systems, adaptive control, nonlinear control, and real-time systems.



Kanty Rabenorosa received the M.S. degree in electrical engineering from Institut National des Sciences Appliquées Strasbourg, Strasbourg, France, in 2007, and the Ph.D. degree in automatic control from the University of Franche-Comté, Besançon, France, in 2010. He was a Post-Doctoral Fellow at Laboratoire d'Informatique, de Robotique et de Micro-électronique de Montpellier, University of Montpellier, France, from 2011 to 2012. He is currently an Associate Professor with the AS2M Department, FEMTO-ST Institute, Besançon. His research interests include mechatronics, smart actuator, soft and continuum micro-robotics for medical applications within the Micro-NanoRobotics team.